Enhanced trace element mobilization by Earth's ice sheets

Jon R. Hawkings[a,b,1], Mark L. Skidmore[c], Jemma L. Wadham[d], John C. Priscu[e], Peter L. Morton[a], Jade E. Hatton[f], Christopher B. Gardner[g], Tyler J. Kohler[h], Marek Stibal[i], Elizabeth A. Bagshaw[j], August Steigmeyer[c], Joel Barker[k], John E. Dore[e], W. Berry Lyons[g], Martyn Tranter[d], Robert G. M. Spencer[a], and the SALSA Science Team[2]

[a]National High Magnetic Field Laboratory Geochemistry Group, Department of Earth, Ocean and Atmospheric Sciences, Florida State University, Tallahassee, FL 32306; [b]Interface Geochemistry, German Research Centre for Geosciences (GFZ), 14473 Potsdam, Germany; [c]Department of Earth Sciences, Montana State University, Bozeman, MT 59717; [d]School of Geographical Sciences, University of Bristol, Bristol, BS8 1SS, United Kingdom; [e]Department of Land Resources and Environmental Sciences, Bozeman, Montana State University, MT 59717; [f]School of Earth Sciences, University of Bristol, Bristol, BS8 1RL, United Kingdom; [g]School of Earth Sciences, Byrd Polar and Climate Research Center, The Ohio State University, Columbus, OH 43210; [h]Stream Biofilm and Ecosystem Research Laboratory, School of Architecture, Civil and Environmental Engineering, École Polytechnique Fédérale de Lausanne, Lausanne CH-1015, Switzerland; [i]Department of Ecology, Faculty of Science, Charles University, CZ-12844, Prague, Czechia; [j]School of Earth and Ocean Sciences, Cardiff University, Cardiff, CF10 3AT, United Kingdom; and [k]Department of Earth and Environmental Sciences, University of Minnesota, Minneapolis, MN 55455

Edited by Donald E. Canfield, Institute of Biology and Nordic Center for Earth Evolution, University of Southern Denmark, Odense M., Denmark, and approved October 13, 2020 (received for review July 8, 2020)

Trace elements sustain biological productivity, yet the significance of trace element mobilization and export in subglacial runoff from ice sheets is poorly constrained at present. Here, we present size-fractionated (0.02, 0.22, and 0.45 μm) concentrations of trace elements in subglacial waters from the Greenland Ice Sheet (GrIS) and the Antarctic Ice Sheet (AIS). Concentrations of immobile trace elements (e.g., Al, Fe, Ti) far exceed global riverine and open ocean mean values and highlight the importance of subglacial aluminosilicate mineral weathering and lack of retention of these species in sediments. Concentrations are higher from the AIS than the GrIS, highlighting the geochemical consequences of prolonged water residence times and hydrological isolation that characterize the former. The enrichment of trace elements (e.g., Co, Fe, Mn, and Zn) in subglacial meltwaters compared with seawater and typical riverine systems, together with the likely sensitivity to future ice sheet melting, suggests that their export in glacial runoff is likely to be important for biological productivity. For example, our dissolved Fe concentration (20,900 nM) and associated flux values (1.4 Gmol y^{-1}) from AIS to the Fe-deplete Southern Ocean exceed most previous estimates by an order of magnitude. The ultimate fate of these micronutrients will depend on the reactivity of the dominant colloidal size fraction (likely controlled by nanoparticulate Al and Fe oxyhydroxide minerals) and estuarine processing. We contend that ice sheets create highly geochemically reactive particulates in subglacial environments, which play a key role in trace elemental cycles, with potentially important consequences for global carbon cycling.

biogeochemical cycles | ice sheets | trace elements | elemental cycles | Southern Ocean

Ice sheets cover almost 10% of Earth's land surface area at present, up to 30% during the last glacial maximum, and account for ∼99% of land ice mass, yet relatively little is known about the biogeochemical conditions beneath them and their importance in polar biogeochemical cycles (1). Both the Greenland Ice Sheet (GrIS) and the Antarctic Ice Sheet (AIS) are undergoing rapid change due to the disproportionate impact of climatic warming in the polar regions, with annual runoff and solid ice discharge contributing ∼1 mm of sea-level rise equivalent per year over the last decade (2, 3). Extensive subglacial hydrological networks exist beneath both ice sheets, including saturated sediments, distributed and channelized water flow paths ("rivers" under ice), and interconnected subglacial lakes that drain into the ocean (4–8). These subglacial hydrological systems support elevated rates of biogeochemical weathering relative to global riverine values (9, 10). High elemental yields from glacial catchments are thought to be sustained by an abundant supply of highly reactive comminuted rock flour with reactive mineral surfaces, produced from high physical erosion rates and elevated rock:water ratios at the ice–rock/sediment interface (11, 12).

Ice sheet subglacial meltwaters have recently been identified as important sources of reactive sediment, solute, and nutrients to downstream ecosystems (13–16), highlighting a potentially important yet poorly understood contribution to global carbon cycling (1). The majority of samples have been collected from comparatively accessible glacial field sites, with extremely limited data available from Antarctic subglacial environments due to extreme technological and logistical challenges of access (17, 18). Given the paucity of data, we do not understand the implications of changing ice sheet melt for biogeochemical cycling in the polar regions and their impact on local and regional processes (19).

Trace element (TE; elements present at low "dissolved" (d) concentrations in natural waters, operationally usually <50 ppb)

Significance

Trace elements are integral to biogeochemical processes at the Earth's surface and play an important role in the carbon cycle as micronutrients to support biological productivity. We present data from the Greenland and Antarctic ice sheets to demonstrate the importance of subglacial biogeochemical processes in mobilizing substantial quantities of these elements. Usually immobile elements are found in subglacial meltwaters at elevated concentrations compared with typical rivers, with most exhibiting distinctive size fractionation due to adsorption onto nanoparticles. Our findings suggest that ice sheets need to be included in models of global biogeochemical cycles of trace elements and studies of the fertilization of adjacent marine systems, especially the Southern Ocean, due to large export fluxes of micronutrients, most notably iron.

Author contributions: J.R.H., M.L.S., J.L.W., and J.C.P. designed research; J.R.H., M.L.S., J.C.P., P.L.M., J.E.H., C.B.G., T.J.K., M.S., E.A.B., A.S., J.B., J.E.D., W.B.L., M.T., and S.S.T. performed research; P.L.M. contributed new reagents/analytic tools; J.R.H. analyzed data; and J.R.H., M.L.S., J.L.W., J.C.P., M.T., and R.G.M.S. wrote the paper with contributions from all other co-authors.

The authors declare no competing interest.

This article is a PNAS Direct Submission.

[1]To whom correspondence may be addressed. Email: jhawkings@fsu.edu.

[2]A complete list of the SALSA Science Team members can be found in the *SI Appendix*.

This article contains supporting information online at https://www.pnas.org/lookup/suppl/doi:10.1073/pnas.2014378117/-/DCSupplemental.

First published November 23, 2020.

concentrations in glacial meltwaters have received minor attention to date (15, 20, 21). The concentration and speciation of TEs may provide important information about the chemical weathering environment, redox processes, water sources, and subglacial hydrological pathways that are not always apparent using only major ion chemistry (22–24), although the source, speciation, transformation, and coassociation of many TEs are still not well understood. For example, Al and V (and to a lesser degree, Ba) can be used as tracers of silicate weathering intensity (25). Mo, Cd, and Zn are strongly chalcophilic elements, and their presence is indicative of oxidation of sulfide minerals (26, 27). Fe and Mn are redox sensitive, and therefore, their presence and speciation indicate reducing source waters and elucidate oxidation rates (28). A number of TEs (e.g., Ni, Co, Pb, and Cr) are siderophiles, and therefore, their mobility can provide information of weathering, transport, and form of Fe and by association, biologically mediated redox processes (29). U can be used as a tracer of oxidative weathering and is sourced mainly from sedimentary rocks (30), while Sr concentrations can be an excellent indicator of carbonate mineral weathering (31). Furthermore, many TEs are biologically essential micronutrients that play critical roles in cellular processes, including C, N, and P transport and assimilation, and as components of metabolic coenzymes/metalloproteins [e.g., Fe, Mn, Mo, Co, Zn, Cu, Cd, Mo, V (32–34)]. Consequently, their export from ice sheets to downstream ecosystems can have important implications for biological productivity and associated patterns of nutrient limitation and elemental inventories (15, 35, 36). We hypothesize that ice sheets play an important yet poorly constrained role in TE cycling given the elevated chemical erosion rates under large ice masses (9, 37, 38), the unique biogeochemical weathering environment (*SI Appendix*, Table S1) in subglacial hydrological systems and the large and increasing ice sheet freshwater export. Constraining TE export from ice sheets is critical for understanding downstream elemental cycling and associated ecosystem response and the implications of future changes to glacial meltwater discharge.

We present size-fractionated TE concentration data (<0.02 μm, "soluble," s[element]; <0.45, dissolved, d[element]; 0.02 to 0.45 μm, "colloidal/nanoparticulate," cn[element]) for subglacial meltwaters sampled beneath the AIS (Mercer Subglacial Lake [SLM], a hydrologically active subglacial lake) and emerging from the GrIS (Leverett Glacier [LG], a large ice sheet catchment) (Fig. 1). We use these data to 1) examine how biogeochemical weathering processes and water sources influence the TE geochemistry of the subglacial environment and infer the potential significance of glacially derived TEs to downstream ecosystems surrounding ice sheets, 2) determine the magnitude of colloidal/nanoparticulate phases for the majority of TEs measured, and 3) assess the enrichment/depletion of micronutrients in glacial meltwaters compared with global nonglacial riverine mean values (hereafter referred to as "riverine mean values") and typical seawater concentrations. Our results significantly advance the understanding of biogeochemical processes beneath large ice sheets and highlight the potential importance of meltwaters in global TE inventories.

Results and Discussion

Controls on TE Composition of AIS and GrIS Meltwaters. Elemental concentrations in SLM and LG waters span an extremely large range with clear patterns of size fractionation in the dissolved <0.45-μm phase (dTE) (Figs. 2 and 3 and *SI Appendix*, Table S1). Data from both locations indicate that the dominant dTEs in subglacial meltwaters are those typically associated with lithogenic weathering of the more abundant elements in the Earth's crust and oxyhydroxide mineral phases (i.e., dAl, dFe, and dTi) with concentrations higher than the mean of nonglacial rivers (Fig. 2*B* and *SI Appendix*, Table S1). For example, dFe concentrations in LG and SLM were up to an order of magnitude higher than mean riverine waters (2,390 and 20,900 nM compared with 1,180 nM), dTi concentrations were at least one order of magnitude higher (277 and 2,080 nM in LG and SLM waters, respectively, compared with ∼10 nM riverine mean), and dAl concentrations at LG and SLM (351 to 105,000 nM) are similar only to concentrations reported in GrIS meltwaters [300 to 13,600 nM (21)]. The elevated concentrations of typically less mobile elements point to the influence of biogeochemical weathering processes in waters with a high pH (up to 9.6 at LG and 8.2 at SLM) (*SI Appendix*, Table S1). The high concentrations of these elements also reflect the importance of physical weathering processes generating an abundant supply of microparticles and predominance of refractory primary minerals and nanoparticulate oxyhydroxides, as observed previously in glacial meltwaters (23, 40, 41), despite the low temperatures (∼0 °C) commonly associated with suppressed weathering rates. These weathering processes hold even within SLM where subglacial water residence times are prolonged [approximately years (42)], underlying sediments are of contrasting origin (overridden marine sediments vs. freshly crushed shield bedrock), and suspended sediment concentrations (SSCs) are relatively low (∼20 mg L^{-1} at SLM vs. ∼1,000 mg L^{-1} at LG), indicating lower local physical erosion rates and turbulence.

The predominant driver of TE composition in these subglacial systems appears to be the weathering of silicate minerals, as elucidated from the abundance of TEs commonly sourced from silicate weathering. For example, V is almost entirely derived from silicate weathering (25), and concentrations in ice sheet meltwaters exceeded the riverine mean value (∼14 nM) (24, 25), with LG waters more than twice as concentrated on average (dV 31.1 nM, up to 89.2 nM) and SLM waters more than an order of magnitude higher (dV 265 nM) (Fig. 3 and *SI Appendix*, Table S1). This contrasts with more variable dissolved silicon (Si) concentrations, which are low in LG waters [9.2 to 56.9 μM (44)], with Si likely retained in secondary weathering products (46) while V is not, yet similar to global riverine concentrations of ∼158 μM in SLM (120 to 140 μM) (Fig. 2) (47). Other TEs typically associated with silicate weathering and at much higher abundance in silicate rocks than carbonate rocks are also found at high concentrations in meltwaters from both ice sheets, especially Al, Ti, Co, Cr, and Ni (Fig. 2*B*) (48).

The major ion chemistry of Whillans Subglacial Lake (SLW) adjacent to SLM (Fig. 1) (38) and from GrIS (9, 16, 37, 44) is also consistent with enhanced silicate mineral weathering beneath ice sheets (49). This contrasts older views that silicate mineral weathering was insignificant beneath glacial systems as valley glaciers typically exhibit geochemical signatures of carbonate weathering (9, 12). The principal weathering conditions are likely to be different at the two ice sheet locations. We contend that GrIS waters exhibit silicate weathering signatures because either the underlying bedrock is carbonate poor (37, 50) and/or meltwater residence times are prolonged in larger GrIS catchments (44), enhancing weathering of minerals with slower dissolution kinetics. The high pH of LG meltwaters (up to 9.6) also enhances the solubility of primary aluminosilicate minerals (12). AIS meltwaters exhibit geochemical conditions of waters with long residence times and highly weathered sediments, where reactive minerals have been previously weathered from the rock matrix (38) and where pore waters in the subglacial sediments are likely to provide a concentrated source of solute to lake waters via diffusion (38).

Sr concentrations in LG and SLM meltwaters reinforce this interpretation. Sr is found at high concentrations in carbonate minerals, with Sr^{2+} substituting for Ca^{2+}, and is therefore common in limestones, dolostones, and evaporites. Concentrations of Sr in LG meltwaters are low (51.6 nM) (Fig. 2*A* and *SI Appendix*, Table S1), consistent with previous measurements (50). SLM Sr

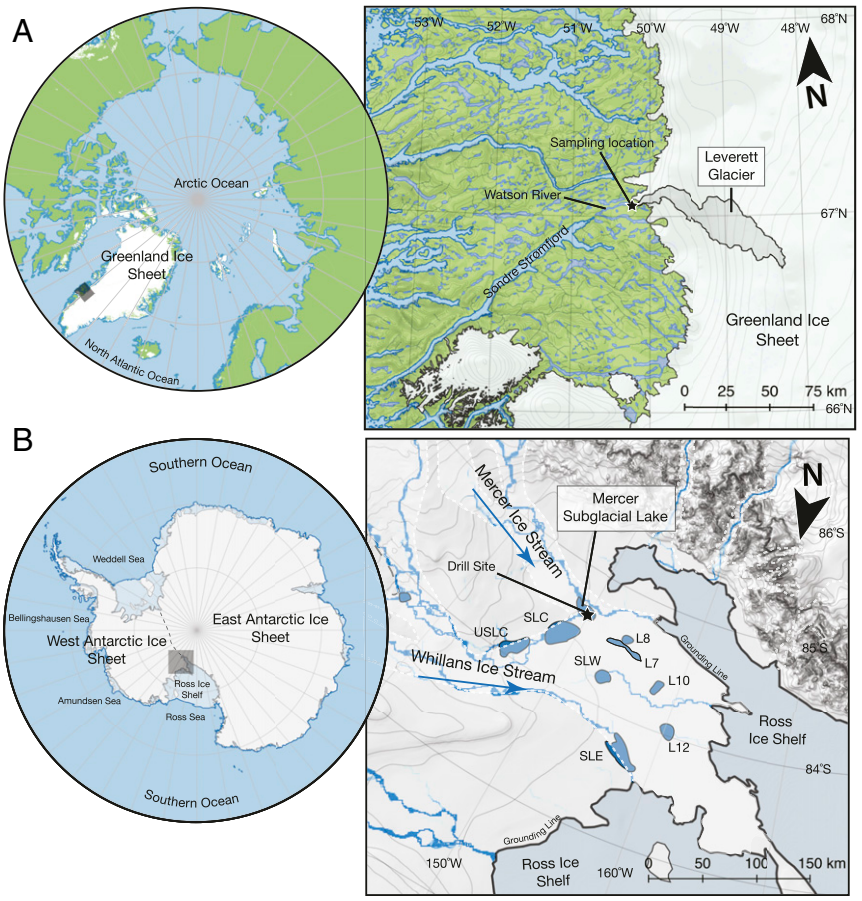

Fig. 1. Map of study regions. (*A*) LG, draining the GrIS, and (*B*) SLM, draining the Mercer Ice Stream. Water flows into the Watson River and then, Søndre Strømfjord in *A*. Modeled water flow paths into the Ross Ice Shelf cavity are indicated by the blue lines in *B* (39). (*Insets*) Polar stereographic maps are cut at (*A*) 60°N and (*B*) 60°S with study areas in shaded boxes. Topographic contours of the ice sheet surface (Greenland) or bed (Antarctic) are at 100-m intervals. L8 . . . 12, lake 8 . . . 12; SLC, Conway Subglacial Lake; SLE, Engelhardt Subglacial Lake; USLC, Upper Conway Subglacial Lake.

concentrations are similar to the riverine mean (~850 vs. 600 to 900 nM) (Figs. 2 and 3) (31) but much lower than riverine catchments where carbonate/evaporitic weathering dominates [e.g., the Colorado River, ~10,000 nM; Rhone and Rhine Rivers, ~6,000 nM; and the Mekong River, ~3,000 nM (31)].

Weathering of sulfide minerals also appears to contribute to meltwater TE composition (38). High cnFe and SO_4^{2-} concentrations in all samples indicate iron sulfide oxidation may be an important weathering pathway for generation of Fe oxyhydroxide nanoparticle aggregates 0.02 to 0.45 μm in size (Fig. 2) (23, 51). The importance of sulfide mineral weathering is reinforced from Mo, a strongly chalcophilic element preferentially weathered from sulfide minerals [predominantly pyrite (26)]. Mo concentrations in LG (1.9 to 11.3 nM) are similar to the global riverine mean [8 nM (26)] and are substantially higher in SLM (52.9 nM) (Figs. 2 and 3).

The Colloidal World of Subglacial Environments. At least 14 of the 17 elements measured have a cn component in glacial meltwaters (Fig. 3 and *SI Appendix*, Table S1). TEs can be broadly separated into three operationally defined classifications (Fig. 3): (Group 1) those strongly associated with the cn phase (>75% cn), (Group 2) those moderately associated with the cn phase but with a significant soluble fraction (≥25 but ≤75% cn), and (Group 3) elements predominantly associated with the soluble phase (<25% cn). SLM and LG meltwaters share nine common Group 1 elements: Ti, Fe, Pb, Co, Ni, Ba, Al, Zn, and Cu; two common Group 2 elements: Cd and V; and three common Group 3 elements: Li, Sr, and Mo. Cr is found mainly in the colloidal phase at both locations but in Group 1 for LG and Group 2 for SLM. U and Mn have contrasting distributions; U is in Group 1 for LG and Group 3 for SLM, while Mn is a Group 1 element at SLM only found in colloidal size fractions, compared with Group 2 at LG, with a substantial proportion (>33%) present as sMn.

Most elements fall into Group 1 in both ice sheet environments (Fig. 3). This phase is likely to consist mostly of inorganic material since dissolved organic carbon (DOC) concentrations are very low at both SLM and LG sampling locations (~30 μM) (*SI Appendix*, Table S1) (45). The large concentrations and proportions of Fe and Al in the cn size fraction (cnFe = 2,390 nM at LG and 20,900 nM at SLM; cnAl = 14,200 nM at LG and 65,000 nM at SLM) (Figs. 2 and 3) indicate that Fe oxyhydroxide nanoparticles (likely ferrihydrite, goethite, and hematite) and Al oxyhydroxide nanoparticles (likely poorly crystalline alumina or gibbsite) control the speciation of these elements via their large adsorption capacity, surface precipitation, or coprecipitation (52). Elements that have an affinity with oxyhydroxide minerals [e.g., Cr, Co, Zn, Ni, and Pb via binding to -OH functional groups (29, 53)], especially just below the oxyhydroxide zero point of charge (pH ~ 9 for Fe oxyhydroxides), are present at much lower concentrations in the soluble phase (<20% of dTE) (Fig. 3). A large sorption capacity of colloidal material for other TEs is also observed in large nonglacial riverine systems, although not to the same degree (53).

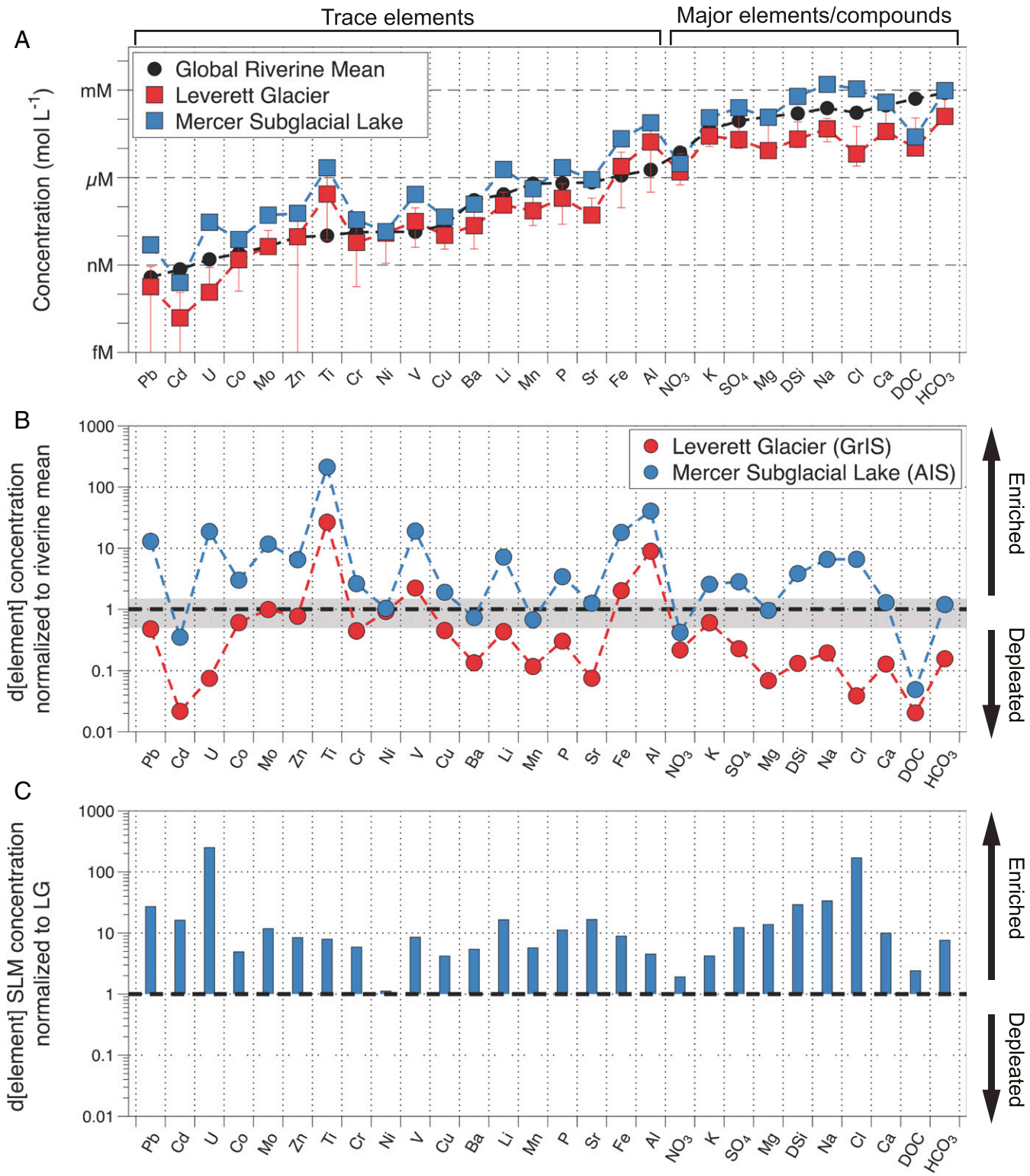

Fig. 2. (*A*) Dissolved (<0.45-μm) mean elemental concentrations on a log scale in LG and SLM samples and either minimum/maximum range (LG) or SDs (SLM), compared with best-estimate mean riverine concentrations (<0.2 to 0.45 μm) (22, 43). (*B*) LG and SLM molar concentrations normalized to the global riverine mean dissolved elemental concentration (22, 43). Values of more than one equal enrichment compared with mean riverine waters. Values less than one indicate depletion compared with mean riverine waters. The gray region indicates values ±50% of the riverine mean. (*C*) Mean SLM concentrations normalized to LG concentrations. LG DOC and major ion/Si data are from refs. 44, 45. Elements are arranged along the *x* axis from lowest mean nonglacial riverine concentration to highest nonglacial mean riverine concentration. N Pb, Cd, and Zn minimum concentrations at LG are below the limit of detection.

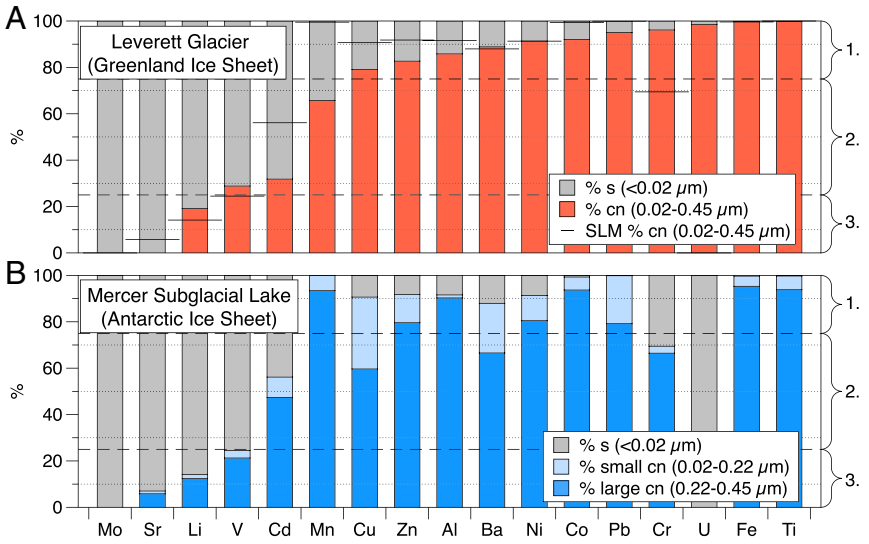

Fig. 3. The proportion of cn and s TE species in ice sheet meltwaters from (*A*) Leverett Glacier (GrIS) and (*B*) Mercer Subglacial Lake (AIS) as a percentage of the <0.45-μm concentration. Ordering from left to right on the *x* axis is according to the percentage of the <0.45-μm fraction that is filterable through a 0.02-μm pore size (i.e., our best approximation of truly dissolved species) in GrIS samples, with the highest on the left and lowest on the right. Elemental groupings are indicated on the right and with the horizontal dashed lines, and they are detailed in the text.

The unique features of subglacial weathering environments provide an explanation for the predominance of these colloidal/nanoparticulate TE phases. The low temperatures (~0 °C) may aid in slowing the aggregation and aging of nanoparticles into denser, larger-size fractions >0.45 μm in size, with smaller aggregates having a greater adsorption capacity due to their extremely high surface area to volume ratios (54). Additionally, aggregation under higher pH conditions (mean pH was >8, up to 9.6) (*SI Appendix*, Table S1) has been found to generate less ordered porous aggregates with high sorption properties (55).

It is possible that other mechanisms inducing this size fractionation are important. Nanoclays rich in Al and Fe (e.g., allophane) can also adsorb/incorporate less abundant elements (56). Alternatively, the extremely fine size fraction of comminuted sediments allows crushed primary rock material to pass through larger-pore size filter membranes (57), and thus, this phase is more indicative of a weathered bulk bedrock signature (i.e., mobile elements have been leached, leaving relatively immobile elements). It is likely this process would differ for SLM (long residence time) vs. LG (comparatively short residence time), with aged secondary minerals (e.g., nanoclays) dominating in the former and primary minerals or freshly precipitated secondary minerals (e.g., amorphous iron oxyhydroxides) dominating in the latter.

The consideration of the cn size fractions appears to be critical in determining the behavior and concentration of filterable TEs in subglacial meltwaters. For example, the operationally defined filter membrane pore size cutoff has a substantial impact on the observed concentration of TEs in SLM (Fig. 3). In addition to 0.02 and 0.45 μm, 0.22-μm filtered samples were taken from SLM, allowing partitioning between small (0.02 to 0.22 μm; cn^{small}) and large (0.22 to 0.45 μm; cn^{large}) cn species. These data show that colloidal/nanoparticulate phases were more abundant in the larger size fraction. In particular, <10% of cnTi and cnFe is contained in the cn^{small} phase compared with >90% in the cn^{large} phase. The geomicrobiological implications of this partitioning are uncertain as the reactivity of this material is not well understood. Given the very high surface area to volume ratios of these particles, we hypothesize they are highly reactive but likely require more complex and energy-intensive processing before biological uptake. The large difference in concentration between colloidal size fractions likely reflects the aggregation of nanoparticulate material to features >0.2 μm, as observed in high-resolution photomicrographs of glacial suspended sediments (23, 40).

Contrasting TE Cycling under Ice Sheets. Several broad similarities exist in the TE composition of SLM and LG meltwaters despite the contrasting hydrological, geological, and geochemical conditions. Most TEs appear to have a colloidal/nanoparticulate component, as discussed above. Only Sr, Mo, and Li existed predominantly in the soluble phase in both environments likely because they are highly mobile elements (particularly Sr and Mo) with geochemical behavior similar to other alkaline and alkaline-earth cations (Figs. 3 and 4). Additionally, the presence of sMo at similar or elevated concentrations to riverine waters at both field sites also implies contributions from an oxic weathering environment (likely alongside flushing of hypoxic/anoxic stored waters under LG) (26), which is reinforced by mean dissolved O_2 saturation exceeding 100% (with respect to atmospheric O_2) at both sampling sites (*SI Appendix*, Table S1) (58). Subglacial concentrations of dissolved lithogenic TEs associated with the most abundant crustal elements are also high in both meltwaters, as previously discussed.

Several key differences exist between the subglacial meltwaters sampled despite these broad similarities. The major difference between subglacial meltwaters in SLM and emerging from LG is the absolute elemental concentration. Both cnTE and sTE concentrations in SLM meltwaters are generally much higher than in LG meltwaters (up to an order of magnitude) (Fig. 2*C* and *SI Appendix*, Table S1). High concentrations of dTE in AIS subglacial environments have been hypothesized (59) given the long residence time of AIS meltwaters, inputs of solute from underlying sediments (38), no subglacial meltwater dilution from surface meltwater (as with the GrIS) (13, 44), and elevated macronutrient concentrations in SLW (15), but have been supported by little evidence until now. Contrasting hydrological environments are also reflected in the mean specific conductance of meltwaters (a proxy for solute concentration), which differ by more than an order of magnitude (12.6 vs. 272 μS cm^{-1}) (*SI Appendix*, Table S1), as well as differences in major ion composition (9, 38, 44). These differences also highlight the distinct biogeochemical processes

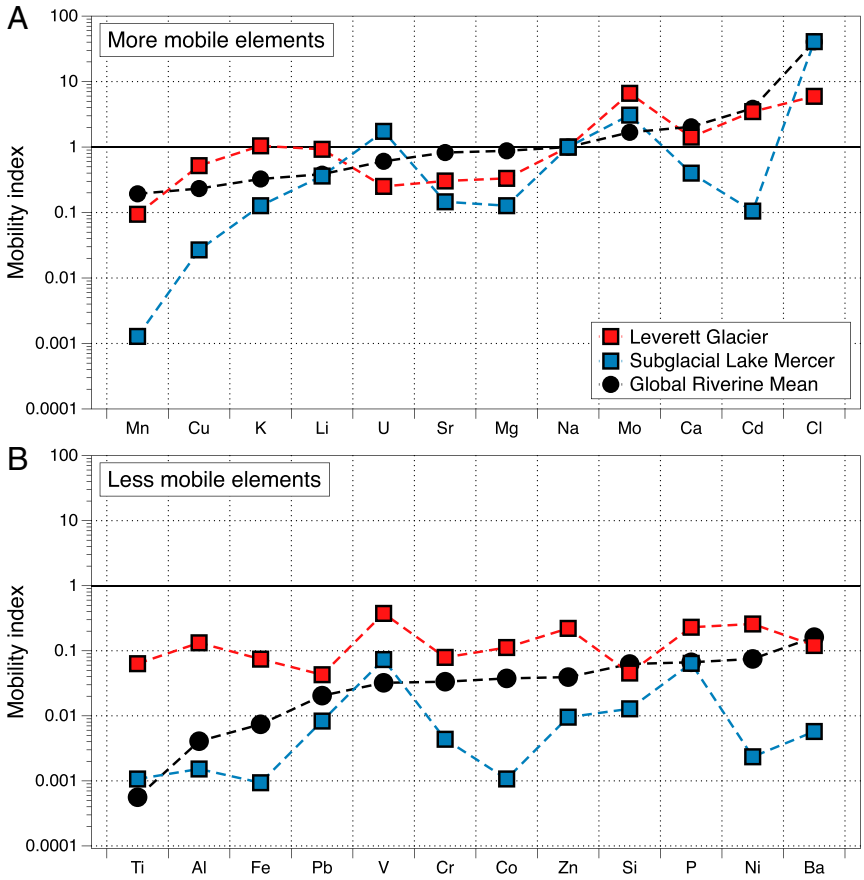

Fig. 4. MIs of (*A*) highly mobile and (*B*) less mobile elements in the dissolved size fraction (<0.45 μm). MI calculated via normalization of dissolved concentrations to upper continental crust abundance (22, 43, 48), with values normalized again to Na (thus, Na = 1 in all environments). Higher values indicate greater elemental mobility from weathering. Elements are grouped and arranged according to mean riverine mobility (22) with least to most mobile elements in the <0.45-μm size fraction going from left to right on the *x* axis.

occurring beneath ice sheets. Enhanced silicate weathering in long-residence time AIS meltwaters produces an abundance of clay minerals and the potential for surficial ion exchange on these clay minerals in long-residence time AIS meltwaters (38). This contrasts with shorter residence times of GrIS meltwaters with rapid silicate hydrolysis and carbonation reactions on freshly crushed primary rock minerals (44) and substantial dilution by incoming fresh supraglacial meltwaters.

The speciation of two TEs highlights some of the variation between ice sheet environments: U (100% sU in AIS but <1% sU in GrIS) and Mn (<1% sMn in AIS but >35% sMn in GrIS). This contrasting behavior is somewhat surprising given the broad similarities observed between other TEs. The behavior of U may relate to the sediment source, with SLM underlain by overridden marine sediments [with U commonly enriched in sedimentary environments (30)] vs. LG sediments generated from Precambrian shield silicate bedrock, likely to be depleted in U (24, 30). SLM waters are also highly enriched in U compared with mean riverine values [29.7 vs. 0.78 nM (30)] (*SI Appendix*, Table S1). Predominance of cnU phases in LG meltwaters may be linked to adsorption onto nanoparticulate Fe oxyhydroxides (60). Evidence of this is given by the lower cnFe:cnU ratio, <5,000, relative to the Fe:U upper continental crust ratio of shield bedrock, ~15,000 (48). No U is associated with the cn fraction at SLM, possibly due to stabilization by ligands (e.g., as $[UO_2(CO_3)_3]^{4-}$) (61) or reflecting the contrasting transport processes (likely grinding of primary rock particles and turbulent water flow at LG vs. diffusion from sediments in SLM).

The absence of sMn in SLM waters vs. LG meltwaters is likely indicative of the longer water residence times [likely to be years (42)] combined with oxidative weathering environment (>100% O_2 saturation with respect to atmospheric O_2) (*SI Appendix*, Table S1). The lack of sMn in SLM waters indicates almost complete oxidation of soluble Mn^{2+} species to insoluble $Mn^{3+/4+}$ and/or adsorption of Mn^{2+} to Mn oxyhydroxides or clays (62). Conversely, in GrIS catchments meltwater transport times through the subglacial drainage systems to the meltwater portal are comparatively rapid [hours to weeks (63)]. Furthermore, isolated hypoxic and anoxic subglacial environments present underneath the GrIS (64) are favorable for generating high point concentrations of sMn (via Mn reduction) and allow persistence of Mn^{2+} despite meltwater being fully oxygenated upon sampling. The half-life of Mn^{2+} in oxygenated waters, before oxidation to Mn^{3+}/Mn^{4+} and precipitation as Mn oxides, is significantly longer than Fe^{2+} in the absence of stabilizing ligands [hours to weeks vs. seconds to minutes (65)], especially at low temperatures, and it appears that soluble Mn^{2+} species persist during transport in the LG subglacial system where stored anoxic/hypoxic subglacial waters are mixed with oxygenated surface meltwater.

TE mobility can also help explain differences between SLM (AIS) and LG (GrIS) chemical weathering environments. Elemental mobility was estimated via a first-order approach (22) by normalization of dissolved concentrations to mean upper continental crust composition (48) and then normalizing to the resulting Na rock:solution ratio so that Na = 1 ("mobility index" [MI]). Our data indicate comparatively low mobility of TE in

SLM meltwaters vs. relatively high mobility in LG meltwaters compared with nonglacial rivers (Fig. 4). Highly chemically weathered sediments underlie SLM; consequently less mobile elements (MI < 1) (Fig. 4*B*) are more likely incorporated into secondary weathering products, likely clay minerals >0.45 μm in size via adsorption/ion exchange and/or coprecipitation (38, 66), and highly mobile elements (MI > 1) (Fig. 4*A*) are likely retained in solution. In contrast, typically less mobile elements (MI < 1) generally have higher mobility in LG meltwaters than both SLM and mean riverine waters, likely reflecting hydrolysis of primary rock minerals after comminution (44).

Finally, LG meltwaters exhibit large variability in TE concentrations driven by seasonal changes in the subglacial drainage system in response to surface meltwater forcing (44, 63, 67). It is currently unknown if there is substantial temporal variation in meltwater composition in SLM or under AIS more widely. Any TE geochemical variability in SLM would be likely to reflect drain/refill cycles in the lake (42), the geochemical consequences of which are unknown but unlikely to be as large as the variation observed in meltwater emerging from LG, given the significant seasonal hydrochemical evolution of GrIS catchments (44).

Implications for Downstream Biogeochemical Cycling. Several TEs are essential micronutrients for microbiota, serving as important components of (co-)enzymes and performing essential roles in cellular processes such as nitrogen and carbon fixation (32). The most important TEs for microbial metabolism are thought to be Fe, Mn, Mo, Co, Zn, Cu, Ni, V, and Cd (32, 33), several of which can be limiting or colimiting for photoautotrophic and heterotrophic activity in marine (35, 68) and freshwater ecosystems (36). Recently, ice sheets have been hypothesized to be significant sources of Fe to the ocean, with high concentrations of dFe found in meltwaters from the GrIS (23, 51, 69, 70) and (sub-)Antarctic maritime islands (71, 72), as well as significant quantities of labile particulate Fe rafted in icebergs (73, 74). Limited data exist for glaciated environments, apart from spot samples from several Greenlandic glaciers (21) that alluded to high concentrations in meltwater. The two ice sheets deliver >2,000 km^3 of freshwater [i.e., >5% of the riverine freshwater flux (75)] to the ocean each year, and this is increasing. Therefore, a first-order consideration of the associated TE input is important in understanding any influence on biological productivity in polar waters adjacent to the ice sheets and potential nutrient limitation/alleviation. Our discussion focuses on flux estimates "at the gate" where meltwater enters the marine environment (Table 1 and *SI Appendix*, Table S2), but we acknowledge that estuarine processing can drastically modulate the TE flux into the open ocean (76, 77).

Nearly all dissolved micronutrient concentrations are elevated in glacial meltwaters from the GrIS and AIS relative to mean ocean concentrations (*SI Appendix*, Table S1). This contrasts with the relatively low dissolved macronutrient (C, N, and P) concentrations reported previously for GrIS (78, 79) but is consistent with higher concentrations reported beneath AIS (Fig. 2*A*) (15). A notable exception is Cd, which is lower in both GrIS (0.015 ± 0.019 nM) and AIS (0.21 ± 0.011 nM) meltwaters compared with nonglacial riverine waters (0.71 nM) (22) and bulk oceanic waters (0.6 nM) (80). Cd is a highly mobile but rare chalcophilic element, so these low concentrations indicate Cd-bearing sulfides (e.g., zinc sulfides rich in Cd, such as sphalerite, and cadmium sulfides, such as greenockite) are depleted in sediments underlying LG and SLM or reflect an anthropogenic source of the high dCd in rivers (27), which is absent in pristine glacial systems. SLM waters are enriched in all other bioessential TEs with concentrations of dCo, dCu, dFe, dMn, and dZn all more than one order of magnitude higher in SLM waters than marine waters and typically exceed or are similar to mean riverine concentrations (Fig. 2 and *SI Appendix*, Table S1). LG concentrations also exceed bulk oceanic concentrations and are broadly similar to mean riverine concentrations (Fig. 2 and *SI Appendix*, Table S1). LG Mn concentrations appear an order of magnitude lower than riverine concentrations, although they exceed bulk oceanic concentrations by more than two orders of magnitude (72.6 vs. 0.3 nM) (*SI Appendix*, Table S1). Mean riverine Mn concentrations reported also appear biased by a lack of high-quality riverine data and concentration estimates in the Amazon River (which has a disproportionate effect on the mean concentration) that span an order of magnitude [60 to 920 nM (22)]. Moreover, LG dMn concentrations are similar to or exceed many North American rivers [e.g., the Columbia River, ∼10 to 100 nM and the Mississippi, ∼1 to 70 nM (28, 81)].

The relatively high dissolved micronutrient concentrations in ice sheet meltwaters that we measured provide evidence that ice sheet meltwaters could supply a suite of dissolved micronutrients to support biological production in coastal regions surrounding AIS and GrIS (82, 83). Collectively, these large regional ice sheet micronutrient inputs should be considered in future TE biogeochemical models where they are currently absent (68, 84, 85).

AIS Fertilization of the Southern Ocean? Our data have particularly important implications for our understanding of ice sheet fertilization of the Fe-deplete Southern Ocean (86). No size-speciated dTE data from subglacial hydrological systems beneath AIS have been previously obtained, although the enrichment of Fe in AIS meltwaters compared with surrounding oceanic environments has been hypothesized and previously measured at SLW (15, 23, 59, 70). The data we present indicate that meltwater discharge from interconnected subglacial lake hydrological systems draining AIS into coastal embayments is likely to elevate labile Fe concentrations (Fig. 2), supporting previously hypothesized glacial Fe fertilization in coastal regions of the Southern Ocean (70–72, 87, 88). The cnFe concentrations in SLM (20,900 nM) far exceed concentrations in LG and other GrIS meltwaters (50 to 7,500 nM) (*SI Appendix*, Table S1) (51, 69). AIS dFe flux estimates based on SLM concentrations (0.66 to 2.1 Gmol y^{-1}) (Table 1) exceed previous AIS estimates by an order of magnitude (0.02 to 0.32 Gmol y^{-1}) (23, 71) and are similar to GrIS dFe export estimates despite the much lower discharge. The SLM values are also consistent with upper-end AIS subglacial meltwater Fe concentration estimates used in a study (30,000 nM) (89), which produced modeled data of Southern Ocean Fe and primary productivity consistent with observations. Even if estuarine removal in the Siple Coast underneath the Ross Ice Shelf filters 99% of subglacially exported Fe, there is still potential for significant AIS Fe fertilization of coastal ecosystems if these species persist and are labile. A more recent modeling study found limited, more localized fertilization potential of ice shelf meltwater (90), highlighting the complexities of evaluating ice sheet influence on downstream productivity. However, the mechanisms of Fe delivery discussed in that study differ (ice shelf melt vs. subglacial meltwater discharge), meltwater concentrations used were lower, and it remains difficult to disentangle meltwater (direct and indirect) vs. sediment sources (argued by the authors to be more important) in coastal regions where primary productivity is high. Additional field data and biogeochemical modeling are clearly needed to disentangle and constrain the major sources of Fe to the Southern Ocean and the impact of direct (meltwater outflow) vs. indirect (glaciogenic sediments composed in part of material deposited by meltwaters) glacial inputs.

An interesting juxtaposition exists when comparing Fe data from SLM with SLW, where the only comparative concentration estimates for the AIS exist. The dFe concentrations reported for SLW (15) are ∼30 nM, compared with the phase size equivalent (<0.22 μm) measured in SLM of 981 nM. This leads to substantial variability in estimated dFe fluxes to the Siple Coast: 61 kmol y^{-1} (15) compared with 40,000 kmol y^{-1} (*SI Appendix*, Table S2). The

Table 1. Estimates of annual fluxes of size-fractionated TEs from the GrIS and the AIS

Element/variable	Unit	GrIS*			AIS†		
		d	cn	s	d	cn	s
Water flux	$km^3\ y^{-1}$	560 (410–730)‡			65 (32.5–97.5)§		
Al	10^9 mol y^{-1}	**9.2** (0.14–77)	**8.0** (0–74)	**1.31** (0–5.8)	**4.5** (2.1–7.1)	**4.2** (2.1–6.3)	**0.33** (0.15–0.53)
Ba	10^6 mol y^{-1}	**13** (1.3–60)	**11** (0.03–58.4)	**1.4** (0.23–22)	**7.6** (3.6–12)	**6.7** (3.3–10)	**0.91** (0.33–1.8)
Cd	10^6 mol y^{-1}	**0.01** (0–0.05)	**0** (0–0.02)	**0.01** (0–0.04)	**0.02** (0.01–0.02)	**0.01** (0–0.01)	**0** (0–0.01)
Co	10^6 mol y^{-1}	**0.86** (0.05–2.9)	**0.79** (0–2.8)	**0.07** (0.01–2.2)	**0.48** (0.24–0.73)	**0.48** (0.24–0.72)	**0** (0–0)
Cr	10^6 mol y^{-1}	**3.4** (0.08–17)	**3.2** (0.01–17)	**0.13** (0.01–1.6)	**2.2** (1.1–3.4)	**1.5** (0.78–2.3)	**0.68** (0.34–1.0)
Cu	10^6 mol y^{-1}	**5.9** (1.3–31)	**4.7** (0.56–17)	**1.2** (0.57–17)	**2.9** (1.4–4.3)	**2.6** (1.3–3.9)	**0.27** (0.13–0.41)
Fe	10^9 mol y^{-1}	**1.3** (0.02–5.5)	**1.3** (0.02–5.5)	**0.01** (0–0.05)	**1.4** (0.66–2.1)	**1.4** (0.66–2.1)	**0**
Li	10^9 mol y^{-1}	**0.06** (0.03–0.23)	**0.01** (0–0.15)	**0.05** (0.03–0.12)	**0.12** (0.06–0.18)	**0.02** (0.01–0.03)	**0.10** (0.05–0.16)
Mn	10^6 mol y^{-1}	**41** (9.6–380)	**27** (0.15–220)	**14** (2.3–370)	**27** (13–41)	**27** (13–40)	**0.03** (0.01–0.04)
Mo	10^6 mol y^{-1}	**2.4** (0.78–8.3)	**0**	**2.4** (0.78–8.3)	**3.4** (1.7–5.2)	**0**	**3.4** (1.7–5.2)
Ni	10^6 mol y^{-1}	**7.0** (0.48–14)	**6.4** (0–13)	**0.61** (0.25–12)	**0.94** (0.47–1.4)	**0.86** (0.43–1.3)	**0.08** (0.04–0.12)
Pb	10^6 mol y^{-1}	**0.11** (0–0.49)	**0.10** (0–0.48)	**0.01** (0–0.02)	**0.32** (0.16–0.48)	**0.32** (0.16–0.48)	**0**
Sr	10^9 mol y^{-1}	**0.03** (0.02–0.14)	**0**	**0.03** (0.02–0.14)	**0.05** (0.03–0.08)	**0**	**0.05** (0.03–0.08)
Ti	10^6 mol y^{-1}	**160** (2.2–610)	**140** (1.1–600)	**1.2** (0.51–3.7)	**140** (65–210)	**140** (65–210)	**0**
U	10^6 mol y^{-1}	**0.07** (0.02–0.55)	**0.06** (0.02–0.48)	**0** (0–0.07)	**1.9** (0.95–2.9)	**0**	**1.9** (0.95–2.9)
V	10^6 mol y^{-1}	**17** (1.4–65)	**5.0** (0–48)	**12** (1.3–23)	**17** (8.6–26)	**4.2** (2.1–6.3)	**13** (6.5–20)
Zn	10^6 mol y^{-1}	**3.9** (0–20)	**3.9** (0–20)	**0.08** (0–1.5)	**4.7** (2.0–7.9)	**4.3** (2.1–7.2)	**0.38** (0.17–0.63)

Elemental fluxes are presented either as megamoles (10^6 mol) or as gigamoles (10^9 mol) per year. The mean is given in bold, and estimated range/uncertainty is given in parentheses. Flux estimates are presented to two significant figures/decimal places.

*Elemental flux estimates from GrIS are derived from the minimum, discharge-weighted mean, and maximum concentrations measured at LG multiplied by the modeled minimum, mean, and maximum 2007 to 2016 ice sheet meltwater discharge.

†Elemental flux estimates from AIS are derived from the minimum, mean, and maximum concentrations measured at SLM multiplied by the modeled minimum, mean, and maximum AIS discharge.

‡Mean modeled GrIS meltwater discharge over 2007 to 2016 from ref. 2. Minimum is the lowest melt year (2013), and maximum is the largest melt year (2012).

§Modeling basal melt rates from ref. 91 with an SD of ±50%.

Fe export calculated from SLW was estimated to be able to maintain measured microbial activity in the Siple Coast region [based on basic elemental stoichiometry (15)]; therefore, estimates based on SLM concentrations vastly exceed that. Although filter type and pore size are not directly comparable, these differences point to the possibility of substantial spatial or temporal heterogeneity [e.g., fill/drain cycles (42)] in Fe concentrations beneath AIS and/or the influence of filtration artifacts such as membrane clogging and reduction in effective pore size (92). Modeling studies of glacial Fe sources to the Southern Ocean coupled to observations of euphotic zone dFe and chlorophyll *a* concentrations (89, 93) and indirect observations under ice shelves (94) reveal that SLM may be more representative of an enriched AIS subglacial end-member. We do not account for reactive particulate iron concentrations in these estimates [e.g., amorphous ferrihydrite (40)], which were found to be elevated in SLW (15) and are likely to be high in SLM. The potential for high spatial variability, consistency in filtration methodology, and elevated labile particulate Fe clearly demonstrate the need for future coordinated studies on AIS subglacial environments.

Modulating Effects of Estuarine Processing. The significance of subglacial trace micronutrients to downstream ecosystem processes will also depend on their behavior following delivery. Downstream elemental transformations are likely to be complex, with each micronutrient exhibiting unique geochemical characteristics during mixing of freshwater with seawater that vary regionally, including conservative behavior (e.g., Ni, Cu, V, and Mo), nonconservative excess (e.g., Mn, Co, Zn, and Cd), and nonconservative removal (e.g., Fe) (95). The behavior of individual elements will depend on

multiple biogeochemical factors such as organic matter concentration and composition, ligand binding, benthic recycling (e.g., via diffusive pore water fluxes or sediment resuspension), adsorption/desorption from mineral surfaces, and microbial uptake or alteration (such as Mn oxidation) (81, 95). The impact of micronutrients on downstream ecosystem processes will also depend on the physical features of the downstream environment. Meltwaters from subglacial environments under the AIS often flow into large subice shelf cavities >400 km from the open ocean with long residence times [several years in the Ross Ice Shelf cavity (15)]. These subice shelf environments will impede immediate delivery of micronutrients to photosynthetic primary producers. Nevertheless, our results (Table 1) indicate AIS subglacial meltwaters may still be able to subsidize the micronutrient inventory in coastal regions of the Southern Ocean where high productivity has been observed, such as pelagic regions proximal to the Ross Ice Shelf downstream of Siple Coast inputs (*SI Appendix*, Table S2), and other major ice streams (83). Conversely, GrIS meltwaters enter coastal regions either as turbid meltwater rivers emerging from land-terminating glaciers or via injection into fjord at depth from tidewater glaciers. These two delivery mechanisms have been observed to drastically alter the biogeochemical conditions for primary producers and surface macronutrient concentrations, but little information is currently available on micronutrient behavior in fjords (19, 82, 96).

The presence of high colloidal TE concentrations in subglacial meltwater is likely to have significant implications for downstream transport and lability. These implications are especially important for Fe, where cnFe will aggregate, flocculate, and be scavenged from the water column at low salinities, with implications for TEs associated with Fe. For example, >95% of dFe is removed in low-salinity regions of Alaskan and Greenlandic estuaries/fjords, but comparatively high concentrations still remain at seawater salinities close to the coast because of the high glacial meltwater end-member concentrations (76, 77). The very high dFe concentrations observed in SLM indicate potential for long-distance transport of glacially derived iron even with large removal rates. The bioavailability of colloidal species is also uncertain as they represent a complex mixture of organic and inorganic material with varying labilities. Soluble species are likely the best empirical measurement of potentially bioavailable phases yet represent a very small fraction of the total dissolved pool (Fig. 3). Colloidal species of trace metals appear more important than soluble species in supply and removal processes in oceanic and coastal systems (97), and this will almost certainly depend on the mineralogy of the colloid/nanoparticles usually included in the filterable fraction (41).

Conclusions

Ice sheets export globally significant quantities of TEs in subglacial meltwaters and as such, should be considered an important component of polar biogeochemical cycling of TEs. TEs in meltwaters sampled from the GrIS and AIS are derived mainly from the biogeochemical weathering of silicate and sulfide minerals, consistent with previous research on major ion composition and mineralogy (9, 38, 44, 46) and further highlighting the potentially important role of ice sheets in enhanced silicate weathering and long-term carbon drawdown (49). Concentrations of TEs in subglacial meltwaters are generally high despite low temperatures, which likely reflects weathering of rock microparticles and/or long water residence times in high rock:water subglacial drainage systems. The importance of colloidal/nanoparticulate species depends on the element in question, but our data indicate a prevalence of elemental species 0.02 to 0.45 μm in size compared with truly soluble (<0.02-μm) aqueous species. Nanoparticulate oxyhydroxide minerals are therefore important in subglacial environments with a high sorption capacity and have important implications for lability and the ultimate fate of TEs in the downstream cascade. The role of subglacial export of TEs to adjacent/downstream polar ecosystems can elevate micronutrient availability and therefore, the carbon cycle by sustaining or altering biological productivity. Downstream TE transport is especially relevant to Antarctica because biological productivity in the Southern Ocean surrounding the AIS is limited by Fe (86). The significance of these fluxes will depend on subice shelf and estuarine processing, which is poorly quantified at present. Our findings have implications for the understanding of elemental cycling during periods of glacial transition, including the increasingly rapid melt of the ice sheets predicted in future climate warming scenarios.

Methods

Study Areas.

SLM (West AIS). AIS samples were collected from December 2018 to January 2019 from SLM (Fig. 1*B*) (84.661°S, 149.677°W) 1,092 m beneath the surface of the West AIS. SLM is one of the largest lakes (136 km^2) beneath Siple Coast ice streams and fed by subglacial waters from the East and West AISs. Approximately 25% of its water is hypothesized to be sourced from beneath the East AIS via Mercer Ice Stream (98). The lake is hydrologically active with multiple drain/fill cycles observed over the past decade (42). The lake depth was 15 m at the time of sampling, and the falling ice elevation indicates the lake was in a draining stage (99). Modeling reveals that downstream flow is through subglacial channels into a marine embayment at the southern reach of the Ross Ice Shelf cavity, with episodic discharge exceeding 300 $m^3\ s^{-1}$ during flood events (7). This region of the West AIS is underlain by glacimarine sedimentary basins (100).

LG (GrIS). GrIS samples were collected from the proglacial river emerging from a subglacial portal exiting LG (67.062°N, 50.201°W) (Fig. 1*A*) (11, 13, 63) in southwest Greenland during the 2015 ablation season. LG is a polythermal-based glacial outlet of GrIS estimated to drain a hydrologically active catchment area of ∼600 to 900 km^2 (11) and is thought to be fairly representative of GrIS land-terminating catchments at large, as detailed elsewhere (13, 64). The LG meltwater river feeds into a larger river system (Watson River) ∼6 km downstream, which discharges into Søndre Strømfjord. Bedrock geology is predominantly Precambrian Shield gneiss/granite, which is the dominant geology under much of GrIS (101).

Sample Collection, Processing, Storage, and Analysis. SLM water samples were retrieved using a standard 10-L Niskin bottle precleaned with 1.2 M HCl (followed by copious rinsing with ultrapure water [UPW]; Milli-Q; 18.2 MΩ cm^{-1}) and 3% H_2O_2 and lowered through an ∼0.6-m-diameter borehole drilled using a microbiologically clean, hot water drilling system (17, 18). A 10-L Niskin bottle was retrieved in six casts into the lake from 29 December 2018 to 4 January 2019. Bulk LG water runoff samples were collected by hand at least once daily from 1 May to 28 July 2015 ∼1 km downstream of the glacier portal to capture changes in subglacial hydrology (67) as detailed below.

TE sampling, processing, and storage. Samples for TE analysis were collected cleanly according to strict size-fractionated TE protocols (23, 92) (procedural blanks are detailed in *SI Appendix*, Table S3). All sampling equipment (250- and 15-mL Nalgene low-density polyethylene [LDPE] bottles and polypropylene/polyethylene [PP/PE] syringes) were cleaned sequentially in 1% Decon 90 (overnight), 6 M HCl (48 h), and 3 M HNO_3 (48 h), with copious rinsing in UPW in between washes and final drying in a laminar flow hood (ISO 5). Whatman GD/XP PES (polyethersulfone) 0.45-μm, Millex-GP Millipore Express 0.22-μm (PES; only SLM), and Whatman Anotop 25 0.02-μm syringe filters were cleaned with ultratrace metal-grade HCl (Optima). The 0.22- and 0.45-μm syringe filters were cleaned by passing through 20 mL of 1.2 M HCl, with the final ∼1 mL allowed to sit in the filter for ∼2 h before rinsing with 40 mL of UPW and flushing with laminar flow-filtered air to dry. The 0.02-μm filters were cleaned by passing 20 mL of 0.02 M HCl, followed immediately by 20 mL of UPW and clean laminar flow-filtered air to dry.

Bulk water samples were collected in 1,000-mL LDPE bottles (Nalgene) from a 10-L Niskin bottle in a field chemistry laboratory at the SLM drill site. Water samples from the Niskin were decanted into a 250-mL LDPE bottle inside a laminar flow hood. The laminar flow hood was previously lined with polyethylene sheeting that had been wiped with 1 M HCl followed by three times wipes with UPW. The sample was then decanted via gravity feed through 1 M HCl rinsed silicone tubing. Approximately 1 to 2 L of lake water from the Niskin bottle was flushed through the tubing before final collection of the TE sample. Personnel conducting the sample decanting and filtration wore full Tyvek clean room suits and polyethylene gloves. Bulk water samples at LG were collected from a fast-moving section at the side of the main proglacial river ∼2 km downstream of the glacier portal (Fig. 1) (23) into 250-mL LDPE bottles (Nalgene; triple rinsed with bulk sample water),

ziplock bagged, and taken immediately to a designated "clean" laboratory tent. Filtration was performed within a laboratory-made filtration box at LG, a large polypropylene box with one face removed and replaced with LDPE sheeting that was taped to the box in between use, thus minimizing potential contamination by dust.

Bulk samples were filtered through the 0.45-μm syringe filter (12 mL to waste/rinse, with final 10 mL collected) and then, through a stack of 0.45-μm/0.02-μm syringe filters (12 mL to waste/rinse with final 10 mL collected). Samples were additionally filtered through the 0.22-μm syringe filters at SLM (12 mL to waste with final 10 mL collected). Samples were preserved in the field at LG by acidifying with Optima HNO_3 to a pH < 2. Samples for TE from SLM were collected from casts 1 to 3, acidified with twice laboratory-distilled ultratrace metal-grade HNO_3 ∼3 mo after collection in a Class 100 clean laboratory, and left acidified at room temperature for 6 wk before analysis. Field blanks for LG were processed in the field with transported UPW identically to samples. Niskin bottle blanks were prepared in the Crary Laboratory, McMurdo Station, Antarctica, before field deployment at SLM. A 10-L Niskin was filled with UPW, left to sit for ∼30 min, and then processed as per samples.

A common concern with TE is contamination during sampling, especially when new sampling methods are used (as at SLM). We are confident that hot water drilling introduced minimal contamination at SLM. First, the water level in the borehole was reduced to lower the head pressure in the borehole. Back pressuring the borehole in this manner allowed the lake water to rise upward of 14 m into the borehole after breakthrough, avoiding potential contamination of the lake by drill water entering the lake water cavity. Specific conductivity and temperature profiles from a conductivity/temperature/depth instrument cast into the lake after drilling, but prior to water sampling, showed no evidence for drill water incursion into the 15-m-deep lake. Second, much of the water in the borehole originates from melting of the ice sheet side wall, not hot water injected into the borehole from the drill. Procedural blanks taken from an access port on the hot water drilling system of the borehole return water [Port 9 (18)] were very low compared with measured values from the lake water (*SI Appendix*, Table S3), with the exception of Zn, where blanks were ∼40 nM (i.e., 55% of the dZn value at SLM). Finally, the Niskin bottle was slowly lowered to middepth in the lake water column (lake water column = 15-m deep); hence, the bottle passed through ∼7.5 m of lake water, flushing it with more than 8 vol of lake water before samples were collected.

TE analytical procedures. SLM samples were measured on a Thermo Scientific Element 2 high-resolution inductively coupled mass spectrometer, and LG samples were measured on a Thermo Scientific XSERIES 2 quadrupole inductively coupled mass spectrometer with collision/reaction cell. Be (beryllium), In (indium), and Re (rhenium) were used as internal standards to correct for drift and matrix effects (only In was used for SLM samples), and eight multielement external calibration solutions were made gravimetrically to match the concentration range observed in samples. Measurement accuracy and precision were checked against reference material NIST1643 (SLM), SLRS-5 (LG), or SLRS-6 (SLM; National Research Council of Canada) and replicate intermediate standards. Analytical precision ranged from ±0.7 to ±8.9% based on replicates of the SLRS-5 and a gravimetrically weighed intermediate standard (n = 6 per run) (*SI Appendix*, Table S4) and ±0.5 to ±7.9% based on replicates of SLRS-6 (n = 5 per run) (*SI Appendix*, Table S5). There were two outliers to this with Cd and Zn being difficult to quantify in LG samples, where precision was more than ±25% due to the low concentrations and counts per second (at or close to the instrumental detection limit). Accuracy was better than ±10% for all elements apart from Cd (LG and SLM) and Zn (LG) as detailed in *SI Appendix*, Tables S4 and S5.

Aqueous geochemical sampling, processing, and analysis. The determination of pH, specific conductivity, oxygen, major ion chemistry, DOC concentration, and SSC for samples from LG has been previously described (44, 45, 58). Aqueous geochemical parameters were measured on samples from SLM as follows; pH, casts 2 and 3; specific conductivity and major ion chemistry, casts 1 to 6; DOC, dissolved inorganic carbon (DIC), and alkalinity, casts 1 to 3, 5, and 6; and SSC, cast 1. pH was measured using an Accumet pH electrode connected to an Accumet AB15 pH meter with internal temperature compensation, standardized with Orion Pure Water pH buffers immediately prior to sample measurement. Additional verification of pH was conducted with the CO2sys software (Excel version 1.02) using measured DIC and alkalinity and the freshwater option (salinity = 0) for dissociation constants of carbonic acid (102). Specific conductivity (at 25 °C) was measured using a YSI 3200 conductivity probe connected to a YSI Model 3100 conductivity meter calibrated immediately prior to sample measurement. Samples for major ion chemistry were vacuum filtered through 0.4-μm Nuclepore membranes into clean 60-mL high-density polyethylene bottles, prerinsed with filtered sample, and stored frozen until analysis. Major ion concentrations were determined on a Metrohm 930 Compact IC Flex ion chromatograph using Metrosep C4 cation and A SUPP 5 anion columns (38). SSC was determined gravimetrically using a preweighed Nuclepore membrane, after drying at 40 °C for 16 h. Alkalinity was measured by acid neutralization to pH 4.5 using bromocresol green-methyl red indicator powder pillows (Permachem reagent 94399) to detect the end point. A micropipette was used to dispense microliter volumes of 0.16 N H_2SO_4 into an ∼25-mL lake water sample. Volumes of acid and lake water were determined gravimetrically. DIC was measured by infrared gas analysis of acid-sparged subsamples from aliquots collected in gas-tight serum vials. Samples for determination of DOC concentrations were filtered, stored, and analyzed as described in ref. 15. Oxygen concentrations were measured using a modified Winkler titration [Limnological Methods for the McMurdo Long Term Ecological Research Program (103)].

Data Availability. All study data are included in the article and *SI Appendix*.

ACKNOWLEDGMENTS. This research is part of European Commission Horizon 2020 Marie Skłodowska-Curie Actions Fellowship ICICLES (Iron and Carbon Interactions and Biogeochemical CycLing in Subglacial EcosystemS) Grant 793962 (to J.R.H.). Antarctic work was funded under the Subglacial Antarctic Lakes Scientific Access (SALSA) project through US NSF Grants 1543537 (to M.L.S., J.C.P., and J.E.D.) and 1543453 (to W.B.L.). The Greenland research was funded by UK Natural Environment Research Council Standard Grant NE/I008845/1 (to J.L.W. and M.T.), Leverhulme Trust Research Grant RPG-2016-439 (to J.L.W.), and a Royal Society Wolfson Merit Award (to J.L.W.). A.S. was supported by NASA Earth and Space Science Fellowship 80NSSC18K1266. We thank all those involved with fieldwork at Leverett camp and the SALSA project. We thank A. Chiuchiolo for conducting DIC analysis for SALSA; analytical support from Dr. M. Cooper at the National Oceanography Centre, United Kingdom, Plasma Mass Spectrometry Laboratory; and G. White in the geochemistry group at the National High Magnetic Field Geochemistry Laboratory, which is supported by NSF Grant DMR-1644779 and the State of Florida. We are grateful for the comments and input from T. Vick-Majors, R. Venturelli, and G. Lamarche-Gagnon on an earlier draft of the manuscript.

1. J. L. Wadham *et al*., Ice sheets matter for the global carbon cycle. *Nat. Commun.* **10**, 3567 (2019).
2. J. L. Bamber, R. M. Westaway, B. Marzeion, B. Wouters, The land ice contribution to sea level during the satellite era. *Environ. Res. Lett.* **13**, 063008 (2018).
3. B. Smith *et al*., Pervasive ice sheet mass loss reflects competing ocean and atmosphere processes. *Science* **368**, 1239–1242 (2020).
4. D. W. Ashmore, R. G. Bingham, Antarctic subglacial hydrology: Current knowledge and future challenges. *Antarct. Sci.* **26**, 758–773 (2014).
5. M. J. Siegert, N. Ross, A. M. Le Brocq, Recent advances in understanding Antarctic subglacial lakes and hydrology. *Philos. Trans. R. Soc. A* **374**, 20140306 (2016).
6. J. S. Bowling, S. J. Livingstone, A. J. Sole, W. Chu, Distribution and dynamics of Greenland subglacial lakes. *Nat. Commun.* **10**, 2810 (2019).
7. S. P. Carter, H. A. Fricker, The supply of subglacial meltwater to the grounding line of the Siple Coast, West Antarctica. *Ann. Glaciol.* **53**, 267–280 (2012).
8. J. C. Priscu *et al*., "Antarctic subglacial water: Origin, evolution, and ecology" in *Polar Lakes and Rivers*, W. F. Vincent, J. Laybourn-Parry, Eds. (Oxford University Press, Oxford, United Kingdom, 2008), vol. 1, pp. 119–137.
9. A. Urra *et al*., Weathering dynamics under contrasting Greenland ice sheet catchments. *Front. Earth Sci.* **7**, 299 (2019).
10. M. Sharp, M. Tranter, Glacier biogeochemistry. *Geochem. Perspect.* **6**, 173–339 (2017).
11. T. Cowton, P. Nienow, I. Bartholomew, A. Sole, D. Mair, Rapid erosion beneath the Greenland ice sheet. *Geology* **40**, 343–346 (2012).
12. M. Tranter, J. L. Wadham, "Geochemical weathering in glacial and proglacial environments" in *Treatise on Geochemistry*, H. D. Turekian, K. K. Holland, Eds. (Elsevier, Oxford, United Kingdom, ed. 2, 2014), pp. 157–173.
13. J. R. Hawkings *et al*., The effect of warming climate on nutrient and solute export from the Greenland Ice Sheet. *Geochem. Perspect. Lett.* **1**, 94–104 (2015).
14. E. Hood, T. J. Battin, J. Fellman, S. O'Neel, R. G. M. Spencer, Storage and release of organic carbon from glaciers and ice sheets. *Nat. Geosci.* **8**, 91–96 (2015).
15. T. J. Vick-Majors *et al*., Biogeochemical connectivity between freshwater ecosystems beneath the West Antarctic ice sheet and the sub-ice marine environment. *Global Biogeochem. Cycle* **34**, e2019GB006446 (2020).
16. J. C. Yde, N. T. Knudsen, B. Hasholt, A. B. Mikkelsen, Meltwater chemistry and solute export from a Greenland ice sheet catchment, Watson River, West Greenland. *J. Hydrol.* **519**, 2165–2179 (2014).
17. J. C. Priscu *et al*., A microbiologically clean strategy for access to the Whillans Ice Stream subglacial environment. *Antarct. Sci.* **25**, 637–647 (2013).

18. A. B. Michaud *et al*., Environmentally clean access to Antarctic subglacial aquatic environments. *Antarct. Sci.* **32**, 329–340 (2020).
19. M. J. Hopwood *et al*., Review article: How does glacier discharge affect marine biogeochemistry and primary production in the Arctic? *Cryosphere* **14**, 1347–1383 (2020).
20. A. C. Mitchell, G. H. Brown, Diurnal hydrological–physicochemical controls and sampling methods for minor and trace elements in an Alpine glacial hydrological system. *J. Hydrol. (Amst.)* **332**, 123–143 (2007).
21. S. M. Aciego, E. I. Stevenson, C. A. Arendt, Climate versus geological controls on glacial meltwater micronutrient production in southern Greenland. *Earth Planet. Sci. Lett.* **424**, 51–58 (2015).
22. J. Gaillardet, J. Viers, B. Dupre, "7.7 - Trace elements in river waters" in *Treatise on Geochemistry (second edition)*, H. D. Holland, K. K. Turekian, Eds. (Elsevier, Oxford, UK, 2014), vol. 5, pp. 195–235.
23. J. R. Hawkings *et al*., Ice sheets as a significant source of highly reactive nanoparticulate iron to the oceans. *Nat. Commun.* **5**, 3929 (2014).
24. C. B. Gardner *et al*., Molybdenum, vanadium, and uranium weathering in small mountainous rivers and rivers draining high-standing islands. *Geochim. Cosmochim. Acta* **219**, 22–43 (2017).
25. A. M. Shiller, L. Mao, Dissolved vanadium in rivers: Effects of silicate weathering. *Chem. Geol.* **165**, 13–22 (2000).
26. C. A. Miller, B. Peucker-Ehrenbrink, B. D. Walker, F. Marcantonio, Re-assessing the surface cycling of molybdenum and rhenium. *Geochim. Cosmochim. Acta* **75**, 7146–7179 (2011).
27. J. T. Cullen, M. T. Maldonado, "Biogeochemistry of cadmium and its release to the environment" in *Cadmium: From Toxicity to Essentiality*, A. Sigel, H. Sigel, R. K. O. Sigel, Eds. (Springer Netherlands, Dordrecht, the Netherlands, 2013), pp. 31–62.
28. A. M. Shiller, Dissolved trace elements in the Mississippi River: Seasonal, interannual, and decadal variability. *Geochim. Cosmochim. Acta* **61**, 4321–4330 (1997).
29. M. M. Benjamin, J. O. Leckie, Multiple-site adsorption of Cd, Cu, Zn, and Pb on amorphous iron oxyhydroxide. *J. Colloid Interface Sci.* **79**, 209–221 (1981).
30. M. R. Palmer, J. M. Edmond, Uranium in river water. *Geochim. Cosmochim. Acta* **57**, 4947–4955 (1993).
31. M. R. Palmer, J. M. Edmond, The strontium isotope budget of the modern ocean. *Earth Planet. Sci. Lett.* **92**, 11–26 (1989).
32. F. M. M. Morel, A. J. Milligan, M. A. Saito, "8.5–Marine bioinorganic chemistry: The role of trace metals in the oceanic cycles of major nutrients" in *Treatise on Geochemistry*, H. D. Holland, K. K. Turekian, Eds. (Elsevier, Oxford, United Kingdom, ed. 2, 2014), pp. 123–150.
33. M. C. Lohan, A. Tagliabue, Oceanic micronutrients: Trace metals that are essential for marine life. *Elements* **14**, 385–390 (2018).
34. B. S. Twining, S. B. Baines, The trace metal composition of marine phytoplankton. *Annu. Rev. Mar. Sci.* **5**, 191–215 (2013).
35. C. M. Moore *et al*., Processes and patterns of oceanic nutrient limitation. *Nat. Geosci.* **6**, 701–710 (2013).
36. T. M. Downs, M. Schallenberg, C. W. Burns, Responses of lake phytoplankton to micronutrient enrichment: A study in two New Zealand lakes and an analysis of published data. *Aquat. Sci.* **70**, 347–360 (2008).
37. J. A. Graly, N. F. Humphrey, C. M. Landowski, J. T. Harper, Chemical weathering under the Greenland ice sheet. *Geology* **42**, 551–554 (2014).
38. A. B. Michaud *et al*., Solute sources and geochemical processes in subglacial lake Whillans, west Antarctica. *Geology* **44**, 347–350 (2016).
39. A. Le Brocq *et al*., Evidence from ice shelves for channelized meltwater flow beneath the Antarctic Ice Sheet. *Nat. Geosci.* **6**, 945–948 (2013).
40. J. R. Hawkings *et al*., Biolabile ferrous iron bearing nanoparticles in glacial sediments. *Earth Planet. Sci. Lett.* **493**, 92–101 (2018).
41. R. Raiswell *et al*., Iron in glacial systems: Speciation, reactivity, freezing behavior, and alteration during transport. *Front. Earth Sci.* **6**, 222 (2018).
42. M. R. Siegfried, H. A. Fricker, Thirteen years of subglacial lake activity in Antarctica from multi-mission satellite altimetry. *Ann. Glaciol.* **59**, 42–55 (2018).
43. J. M. Martin, M. Meybeck, Elemental mass-balance of material carried by major world rivers. *Mar. Chem.* **7**, 173–206 (1979).
44. J. E. Hatton *et al*., Investigation of subglacial weathering under the Greenland Ice Sheet using silicon isotopes. *Geochim. Cosmochim. Acta* **247**, 191–206 (2019).
45. A. M. Kellerman *et al*., Glacier outflow dissolved organic matter as a window into seasonally changing carbon sources: Leverett Glacier, Greenland. *J. Geophys. Res. Biogeosci.* **125**, e2019JG005161 (2020).
46. J. R. Hawkings *et al*., Ice sheets as a missing source of silica to the polar oceans. *Nat. Commun.* **8**, 14198 (2017).
47. H. H. Durr, M. Meybeck, J. Hartmann, G. G. Laruelle, V. Roubeix, Global spatial distribution of natural riverine silica inputs to the coastal zone. *Biogeosciences* **8**, 597–620 (2011).
48. R. L. Rudnick, S. Gao, "Composition of the continental crust" in *Treatise on Geochemistry*, H. D. Holland, K. K. Turekian, Eds. (Elsevier, Oxford, United Kingdom, ed. 2, 2014), pp. 1–51.
49. J. L. Wadham *et al*., Biogeochemical weathering under ice: Size matters. *Global Biogeochem. Cycle* **24**, GB3025 (2010).
50. R. S. Hindshaw, J. Rickli, J. Leuthold, J. Wadham, B. Bourdon, Identifying weathering sources and processes in an outlet glacier of the Greenland Ice Sheet using Ca and Sr isotope ratios. *Geochim. Cosmochim. Acta* **145**, 50–71 (2014).
51. E. I. Stevenson, M. S. Fantle, S. B. Das, H. M. Williams, S. M. Aciego, The iron isotopic composition of subglacial streams draining the Greenland Ice Sheet. *Geochim. Cosmochim. Acta* **213**, 237–254 (2017).
52. V. Barrón, J. Torrent, "9. - Iron, manganese and aluminium oxides and oxyhydroxides" in *Minerals at the Nanoscale*, F. Nieto, K. J. T. Livi, R. Oberti, Eds. (Mineralogical Society of Great Britain and Ireland, Twickenham, UK, 2013), pp. 295–334.
53. G. Olivié-Lauquet, T. Allard, J. Bertaux, J.-P. Muller, Crystal chemistry of suspended matter in a tropical hydrosystem, Nyong basin (Cameroon, Africa). *Chem. Geol.* **170**, 113–131 (2000).
54. J. P. Stegemeier, B. C. Reinsch, C. J. Lentini, J. G. Dale, C. S. Kim, Aggregation of nanoscale iron oxyhydroxides and corresponding effects on metal uptake, retention, and speciation. II. Temperature and time. *Geochim. Cosmochim. Acta* **148**, 113–129 (2015).
55. J. G. Dale, J. P. Stegemeier, C. S. Kim, Aggregation of nanoscale iron oxyhydroxides and corresponding effects on metal uptake, retention, and speciation. I. Ionic-strength and pH. *Geochim. Cosmochim. Acta* **148**, 100–112 (2015).
56. M. F. Hochella Jr. *et al*., Nanominerals, mineral nanoparticles, and Earth systems. *Science* **319**, 1631–1635 (2008).
57. H. Pryer *et al*, The Effects of Glacial Cover on Riverine Silicon Isotope Compositions in Chilean Patagonia. *Frontiers in Earth Science*. DOI: 10.3389/feart.2020.00368, in press.
58. A. D. Beaton *et al*., High-resolution in situ measurement of nitrate in runoff from the Greenland ice sheet. *Environ. Sci. Technol.* **51**, 12518–12527 (2017).
59. J. Wadham *et al*., The potential role of the Antarctic Ice Sheet in global biogeochemical cycles. *Earth Environ. Sci. Trans. R. Soc. Edinburgh* **104**, 55–67 (2013).
60. K.-U. Ulrich, A. Rossberg, H. Foerstendorf, H. Zänker, A. C. Scheinost, Molecular characterization of uranium(VI) sorption complexes on iron(III)-rich acid mine water colloids. *Geochim. Cosmochim. Acta* **70**, 5469–5487 (2006).
61. S. J. Markich, Uranium speciation and bioavailability in aquatic systems: An overview. *ScientificWorldJournal* **2**, 707–729 (2002).
62. K. Saeki, S.-I. Wada, M. Shibata, Ca2+-Fe2+ and Ca2+-Mn2+ exchange selectivitiy of kaolinite, montmorillonite, and illite. *Soil Sci.* **169**, 125–132 (2004).
63. D. M. Chandler *et al*., Evolution of the subglacial drainage system beneath the Greenland Ice Sheet revealed by tracers. *Nat. Geosci.* **6**, 195–198 (2013).
64. G. Lamarche-Gagnon *et al*., Greenland melt drives continuous export of methane from the ice-sheet bed. *Nature* **565**, 73–77 (2019).
65. J. F. Pankow, J. J. Morgan, Kinetics for the aquatic environment–manganese. *Environ. Sci. Technol.* **15**, 1306–1313 (1981).
66. R. D. Cody, Adsorption and the reliability of trace elements as environment indicators for shales. *J. Sediment. Res.* **41**, 461–471 (1971).
67. T. J. Kohler *et al*., Carbon dating reveals a seasonal progression in the source of particulate organic carbon exported from the Greenland Ice Sheet. *Geophys. Res. Lett.* **44**, 6209–6217 (2017).
68. A. Tagliabue *et al*., The role of external inputs and internal cycling in shaping the global ocean cobalt distribution: Insights from the first cobalt biogeochemical model. *Global Biogeochem. Cycles* **32**, 594–616 (2018).
69. M. P. Bhatia *et al*., Greenland meltwater as a significant and potentially bioavailable source of iron to the ocean. *Nat. Geosci.* **6**, 274–278 (2013).
70. P. J. Statham, M. Skidmore, M. Tranter, Inputs of glacially derived dissolved and colloidal iron to the coastal ocean and implications for primary productivity. *Global Biogeochem. Cycle* **22**, GB3013 (2008).
71. A. Hodson *et al*., Climatically sensitive transfer of iron to maritime Antarctic ecosystems by surface runoff. *Nat. Commun.* **8**, 14499 (2017).
72. P. van der Merwe *et al*., High lability Fe particles sourced from glacial erosion can meet previously unaccounted biological demand: Heard Island, Southern Ocean. *Front. Mar. Sci.* **6**, 332 (2019).
73. M. J. Hopwood *et al*., Highly variable iron content modulates iceberg-ocean fertilisation and potential carbon export. *Nat. Commun.* **10**, 5261 (2019).
74. R. Raiswell *et al*., Potentially bioavailable iron delivery by iceberg-hosted sediments and atmospheric dust to the polar oceans. *Biogeosciences* **13**, 3887–3900 (2016).
75. A. Dai, K. E. Trenberth, Estimates of freshwater discharge from continents: Latitudinal and seasonal variations. *J. Hydrometeorol.* **3**, 660–687 (2002).
76. M. J. Hopwood *et al*., Seasonal changes in Fe along a glaciated Greenlandic fjord. *Front. Earth Sci.* **4**, 15 (2016).
77. A. W. Schroth, J. Crusius, I. Hoyer, R. Campbell, Estuarine removal of glacial iron and implications for iron fluxes to the ocean. *Geophys. Res. Lett.* **41**, 3951–3958 (2014).
78. J. L. Wadham *et al*., Sources, cycling and export of nitrogen on the Greenland Ice Sheet. *Biogeosciences* **13**, 6339–6352 (2016).
79. J. Hawkings *et al*., The Greenland Ice Sheet as a hotspot of phosphorus weathering and export in the Arctic. *Global Biogeochem. Cycles* **30**, 191–210 (2016).
80. K. W. Bruland, R. Middag, M. C. Lohan, "Controls of trace metals in seawater" in *Treatise on Geochemistry*, H. D. Holland, K. K. Turekian, Eds. (Elsevier, Oxford, United Kingdom, ed. 2, 2014), pp. 19–51.
81. K. W. Bruland *et al*., Factors influencing the chemistry of the near-field Columbia River plume: Nitrate, silicic acid, dissolved Fe, and dissolved Mn. *J. Geophys. Res. Oceans* **113**, C00B02 (2008).
82. L. Meire *et al*., Marine-terminating glaciers sustain high productivity in Greenland fjords. *Glob. Change Biol.* **23**, 5344–5357 (2017).
83. K. R. Arrigo, G. L. van Dijken, A. L. Strong, Environmental controls of marine productivity hot spots around Antarctica. *J. Geophys. Res. Oceans* **120**, 5545–5565 (2015).
84. M. van Hulten *et al*., Manganese in the west Atlantic Ocean in the context of the first global ocean circulation model of manganese. *Biogeosciences* **14**, 1123–1152 (2017).
85. C. Richon, A. Tagliabue, Insights into the major processes driving the global distribution of copper in the ocean from a global model. *Global Biogeochem. Cycles* **33**, 1594–1610 (2019).
86. J. H. Martin, S. E. Fitzwater, R. M. Gordon, Iron deficiency limits phytoplankton growth in Antarctic waters. *Global Biogeochem. Cycles* **4**, 5–12 (1990).

87. A. L. Annett *et al*., Controls on dissolved and particulate iron distributions in surface waters of the Western Antarctic Peninsula shelf. *Mar. Chem.* **196**, 81–97 (2017).
88. L. J. A. Gerringa *et al*., Iron from melting glaciers fuels the phytoplankton blooms in Amundsen Sea (Southern Ocean): Iron biogeochemistry. *Deep Sea Res. Part II Top Stud. Oceanogr.* **71-76**, 16–31 (2012).
89. R. Death *et al*., Antarctic ice sheet fertilises the Southern Ocean. *Biogeosciences* **11**, 2635–2643 (2014).
90. R. Person *et al*., Sensitivity of ocean biogeochemistry to the iron supply from the Antarctic Ice Sheet explored with a biogeochemical model. *Biogeosciences* **16**, 3583–3603 (2019).
91. F. Pattyn, Antarctic subglacial conditions inferred from a hybrid ice sheet/ice stream model. *Earth Planet. Sci. Lett.* **295**, 451–461 (2010).
92. A. M. Shiller, Syringe filtration methods for examining dissolved and colloidal trace element distributions in remote field locations. *Environ. Sci. Technol.* **37**, 3953–3957 (2003).
93. C. Laufkötter, A. A. Stern, J. G. John, C. A. Stock, J. P. Dunne, Glacial iron sources stimulate the Southern Ocean carbon cycle. *Geophys. Res. Lett.* **45**, 13377–13385 (2018).
94. L. Herraiz-Borreguero, D. Lannuzel, P. van der Merwe, A. Treverrow, J. B. Pedro, Large flux of iron from the amery ice shelf marine ice to Prydz Bay, East Antarctica. *J. Geophys. Res. Oceans* **121**, 6009–6020 (2016).
95. G. A. Cutter, Trace elements in estuarine and coastal waters–U.S. studies from 1986–1990. *Rev. Geophys.* **29**, 639–644 (1991).
96. M. R. Cape, F. Straneo, N. Beaird, R. M. Bundy, M. A. Charette, Nutrient release to oceans from buoyancy-driven upwelling at Greenland tidewater glaciers. *Nat. Geosci.* **12**, 34–39 (2019).
97. K. Kunde *et al*., Iron distribution in the subtropical North Atlantic: The pivotal role of colloidal iron. *Global Biogeochem. Cycles* **33**, 1532–1547 (2019).
98. S. P. Carter, H. A. Fricker, M. R. Siegfried, Evidence of rapid subglacial water piracy under Whillans ice stream, west Antarctica. *J. Glaciol.* **59**, 1147–1162 (2013).
99. M. R. Siegfried *et al*., "Anatomy of a draining subglacial lake in West Antarctica" in *AGU Fall Meeting* (American Geophysical Union, San Francisco, CA, 2019), https://ui.adsabs.harvard.edu/abs/2019AGUFM.C12A..07S/abstract.
100. S. Anandakrishnan, D. D. Blankenship, R. B. Alley, P. L. Stoffa, Influence of subglacial geology on the position of a West Antarctic ice stream from seismic observations. *Nature* **394**, 62–65 (1998).
101. N. Henriksen, A. K. Higgins, F. Kalsbeek, T. C. R. Pulvertaft, Greenland from Archaean to Quaternary Descriptive text to the 1995 Geological map of Greenland, 1:2 500 000. *Geolog. Surv. Den. Greenl.* **18**, 1–126 (2009).
102. D. Pierrot, E. Lewis, D. W. R. Wallace, "MS Excel program developed for CO2 system calculations" (Rep. ORNL/CDIAC-105, Carbon Dioxide Information Analysis Center, Oak Ridge National Laboratory, U.S. Department of Energy, Oak Ridge, TN, 2006).
103. J. H. Carpenter, The Chesapeake Bay Institute technique for the Winkler dissolved oxygen method. *Limnol. Oceanogr.* **10**, 141–143 (1965).